

# Combined $^7\text{Li}$ NMR, density functional theory and *operando* synchrotron X-ray powder diffraction to investigate a structural evolution of cathode material $\text{LiFeV}_2\text{O}_7$ <sup>†</sup>

Taiana L. E. Pereira,<sup>a</sup> Jon Serrano Sevillano,<sup>bc</sup> Beatriz D. Moreno,<sup>d</sup> Joel W. Reid,<sup>d</sup> Dany Carlier<sup>c</sup> and Gillian R. Goward<sup>id</sup>\*<sup>a</sup>

Received 16th April 2024, Accepted 3rd June 2024

DOI: 10.1039/d4fd00077c

In our recent study, we demonstrated using  $^7\text{Li}$  solid-state Nuclear Magnetic Resonance (ssNMR) and single-crystal X-ray diffraction that the cathode  $\text{LiFeV}_2\text{O}_7$  possesses a defect associated with the positioning of vanadium atoms. We proposed that this defect could be the source of extra signals detected in the  $^7\text{Li}$  spectra. In this context, we now apply density functional theory (DFT) calculations to assign the experimental signals observed in  $^7\text{Li}$  NMR spectra of the pristine sample. The calculation results are in strong agreement with the experimental observations. DFT calculations are a useful tool to interpret the observed paramagnetic shifts and understand how the presence of disorder affects the spectra behavior through the spin-density transfer processes. Furthermore, we conducted a detailed study of the lithiated phase combining *operando* synchrotron powder X-ray diffraction (SPXRD) and DFT calculations. A noticeable volume expansion is observed through the first discharge cycle which likely contributes to the enhanced lithium dynamics in the bulk material, as supported by previously published ssNMR data. DFT calculations are used to model the lithiated phase and demonstrate that both iron and vanadium participate in the redox process. The unusual electronic structure of the  $\text{V}^{4+}$  exhibits a single electron on the  $3d_{xy}$  orbital perpendicular to the  $\text{V}-\text{O}-\text{Li}$  bond being a source of a negative Fermi contact shift observed in the  $^7\text{Li}$  NMR of the lithiated phase.

<sup>a</sup>Department of Chemistry & Chemical Biology, McMaster University, 1280 Main St. West, Hamilton, Ontario L8S 4M1, Canada. E-mail: goward@mcmaster.ca; Tel: +1 905 525 9140 ext. 24176; Web: <https://www.chemistry.mcmaster.ca/goward>

<sup>b</sup>Centro de Investigación Cooperativa de Energías Alternativas (CIC energiGUNE), Basque Research and Technology Alliance (BRTA), 01510 Vitoria-Gasteiz, Spain

<sup>c</sup>CNRS, Bordeaux INP, ICMCB UMR5026, Université Bordeaux, F-33600 Pessac, France

<sup>d</sup>Canadian Light Source, 44 Innovation Boulevard, Saskatoon, SK, S7N 2V3, Canada

<sup>†</sup> Electronic supplementary information (ESI) available. See DOI: <https://doi.org/10.1039/d4fd00077c>

# 1 Introduction

The development and optimization of cathode materials for lithium-ion batteries represent a critical field of research in the search for advanced energy storage solutions. Their performance is intricately related to their chemical structure which may contain crystallographic defects, such as vacancies, antisites, and dislocations, consequently producing disordered systems.<sup>1,2</sup> In various functional materials, structural and compositional defects are unavoidable, especially when considering large-scale production. With advances in characterization techniques, these irregularities have been identified and their effects on physical and chemical properties have been understood. An example of this is olivine  $\text{LiFePO}_4$  (LFP) cathode (theoretical capacity of  $170 \text{ mA h g}^{-1}$ ), which is known for its stability, safety, and long cycle life in lithium-ion batteries. Antisite defects in  $\text{LiFePO}_4$  result in a reduced  $\text{Li}^+$  diffusion rate, causing a negative effect on the electrochemical performance.<sup>1,3</sup> However, in some cases, the defects contribute positively to the electrochemical performance of batteries. Wang *et al.*<sup>4</sup> showed that introducing a considerable number of twin boundary defects into the lattice of spinel lithium manganate oxide ( $\text{LiMn}_2\text{O}_4$ ) lowers the barrier of the lithium diffusion process, consequently improving the lithium-ion diffusion rate.

Different types of defects impact the electrochemical performance of electrode materials to greater or lesser extents, depending on their impact on the framework structure including its stability and the exchangeability of lithium ions in the vicinity of the defects. Detecting and understanding these defects in potential cathode structures is crucial for optimizing the performance and advancing the technology in lithium-ion batteries. In a previous study,<sup>17</sup> a new crystal structure for  $\text{LiFeV}_2\text{O}_7$  was determined by X-ray diffraction that exhibited the presence of disorder, two possible local environments for the vanadium centers. It was found that the V2, V6, and O8 sites shift the position in such a way that the coordination of V2 becomes tetrahedral and V6 trigonal bipyramidal. We hypothesized that the presence of vanadium disorder provides an explanation for the presence of extra signals in the  $^7\text{Li}$  NMR spectra. However, more information is needed to assign the lithium environments to the observed  $^7\text{Li}$  NMR signals. Density functional theory (DFT) calculation has been shown to effectively predict NMR chemical shift assignments and thereby to provide correlations between the local structural details and the resulting Fermi contact shifts.<sup>5–11</sup> Here we combined experimental and theoretical  $^7\text{Li}$  NMR studies of  $\text{LiFeV}_2\text{O}_7$ .

Furthermore, an *operando* and *ex situ* synchrotron powder X-ray diffraction (SPXRD) study of the structural evolution of  $\text{LiFeV}_2\text{O}_7$  during the first discharge cycle was performed at higher energy wiggler beamline of the Brockhouse X-ray Diffraction and Scattering (BXDS) sector at the Canadian Light Source. Previously, a marked enhancement in lithium-ion dynamics was observed after 0.5 mol of  $\text{Li}^+$  was inserted. Here the lithiated structure  $\text{Li}_{1.71}\text{FeV}_2\text{O}_7$  is determined by combining the data obtained from *ex situ* SPXRD and bond valence energy landscape (BVEL) calculations.<sup>12–14</sup> Subsequently, the structure is optimized using DFT calculations to determine all stable atomic positions including new Li sites. This iterative process of modeling is followed by computational validation and

optimization which allow for a robust approximation of the lithium positions within the material's framework, providing a plausible atomic-level understanding of the lithiated phase.

## 2 Experimental methods

### 2.1 VASP calculations

First principles calculations were performed within the density functional theory (DFT). Vienna *ab initio* simulation package (VASP) was chosen to run the calculation utilizing projector augmented wave (PAW) with pseudopotentials.<sup>15,16</sup> We used the standard PAW–Perdew–Burke–Ernzerhof (PBE) potentials for Fe, V, and O and the “sv” PAW–PBE potential for Li that treats the 1s shell as valence states. For Li Fermi contact shift the sv PAW–PBE potential has been shown to yield more accurate results.<sup>7</sup> A plane wave energy cut-off of 750 eV and a K-point grid of  $2 \times 4 \times 2$  were used for all LiFeV<sub>2</sub>O<sub>7</sub> structures. The experimental crystal structure was used as the input model,<sup>17,18</sup> and the calculations were spin polarized type with imposed ferromagnetic ordering which is considered appropriate for the Fermi contact interaction.<sup>5</sup> The energy minimization and electron density for each atom were calculated using two different approaches: the generalized gradient approximation (GGA) and GGA+U method. The GGA+U method incorporates a Hubbard-type interaction to localize d electrons. In this work, *U* values of 3.5, 4.3 and 5.3 eV for Fe and 3.25 eV for V (lithiated structure only) were examined as part of the testing process.

The isotropic shifts were calculated using eqn (1) and a temperature of 320 K to account for typical heating of the rotor during spinning at 60 kHz.

$$\delta_{\text{iso}}(T) = \frac{\chi_{\text{M}}(T)}{3N_{\text{A}}} \cdot \frac{A_{\text{iso}} \cdot S_{\text{tot}}}{\gamma_{\text{N}}} \quad (1)$$

where  $S_{\text{tot}}$  is twice the spin quantum number of the paramagnetic ions in the considered unit cell (*i.e.*, the number of unpaired electrons),  $S$  is theoretical spin per LiFeP<sub>2</sub>O<sub>7</sub> mole,  $\chi_{\text{M}}$  is the molar magnetic susceptibility for LiFeP<sub>2</sub>O<sub>7</sub> formula unit,  $N_{\text{A}}$  is Avogadro's number, and  $\gamma_{\text{N}}$  is the gyromagnetic ratio for the measured nucleus.  $A_{\text{iso}}$  is the hyperfine coupling constant, which is calculated using the VASP program. As the magnetic measurements for this material are not available, we considered for <sup>7</sup>Li Fermi contact shifts calculations, the molar magnetic susceptibility of LiFeP<sub>2</sub>O<sub>7</sub>,<sup>19</sup> which also contains Fe<sup>3+</sup> ions in a rather similar lattice. 3D calculated spin density maps were plotted using VESTA software (visualization for electronic and structural analysis).<sup>20</sup>

### 2.2 Synchrotron X-ray diffraction

**2.2.1 Battery preparation.** The cathode material was prepared by grinding LiFeV<sub>2</sub>O<sub>7</sub> and Super P carbon black (CB) followed by an addition of a solution of 2.0% polyvinylidene fluoride (PVDF) in *N*-methyl-2-pyrrolidone (NMP) in 84 : 10 : 6 weight% ratio. The mixer was left stirring for 2 hours. The resulting slurry was deposited on an aluminum foil current collector using the doctor blade (15 mils) technique. The electrode was dried under a vacuum overnight at 120 °C. The material was punched into discs 1.27 cm in diameter and assembled in modified CR2025 coin cell casings with LiPF<sub>6</sub> (1 M LiPF<sub>6</sub> in a 1 : 1 wt% ethylene carbonate :

diethyl carbonate solution) as the electrolyte, Celgard 2325 as the separator and Li-metal as the negative electrode in an argon-filled glovebox.

For the *operando* Synchrotron Powder X-ray Powder Diffraction (SPXRD) measurement, the coin cells were modified with 5 mm diameter holes at both entry and exit transmission and also in the spacer, as shown in Fig. S1.† The Kapton tape ( $50.8 \pm 2 \mu\text{m}$  thick) was used on both anode and cathode casings to avoid any air contamination. The half-coin cell was discharged on the SRS EC301 Potentiostat from 2.75 V to 2.27 V at a constant current of  $5.45 \times 10^{-2}$  mA (approximately C/20) at room temperature.

**2.2.2 Synchrotron X-ray measurements.** *Operando* powder diffraction measurements were conducted on a half-cell configuration in a modified coin cell on the BXDS higher energy wiggler (HEW) beamline at the Canadian Light Source (CLS). Each pattern was collected using a PerkinElmer XRD 1621 CN3 EHS 2D detector (pixel size  $200 \mu\text{m} \times 200 \mu\text{m}$ ) with an exposure time of 0.8 min. The detector distance, position and tilt were precisely calibrated using a reference standard of Ni powder with GSAS-II, prior to integration of 2D images to point detector patterns from  $3^\circ$  to  $25^\circ$ ,  $2\theta$   $\lambda = 0.3542 \text{ \AA}$ ,  $E = 35 \text{ keV}$ . A pattern was collected every 8 min during the first discharge process and data collection was undertaken at room temperature. GSAS-II software was used for sequential Rietveld refinement of  $\text{LiFeV}_2\text{O}_7$  during electrochemical cycling.<sup>21</sup> For the sequential refinement, the unit cell parameters, iron, vanadium, and oxygen coordinates were allowed to vary. *Ex situ* PXRD was also conducted on the BXDS lower energy wiggler (LEW) beamline.<sup>22</sup> The detector was a Mythen2 X series 1 K strip detector from Dectris mounted on 1.1 m goniometer arm, with a total exposure time of 5.16 min. The wavelength was precisely calibrated using a reference standard of LaB6 powder to be  $\lambda = 0.8193 \text{ \AA}$  (15.1328 keV).

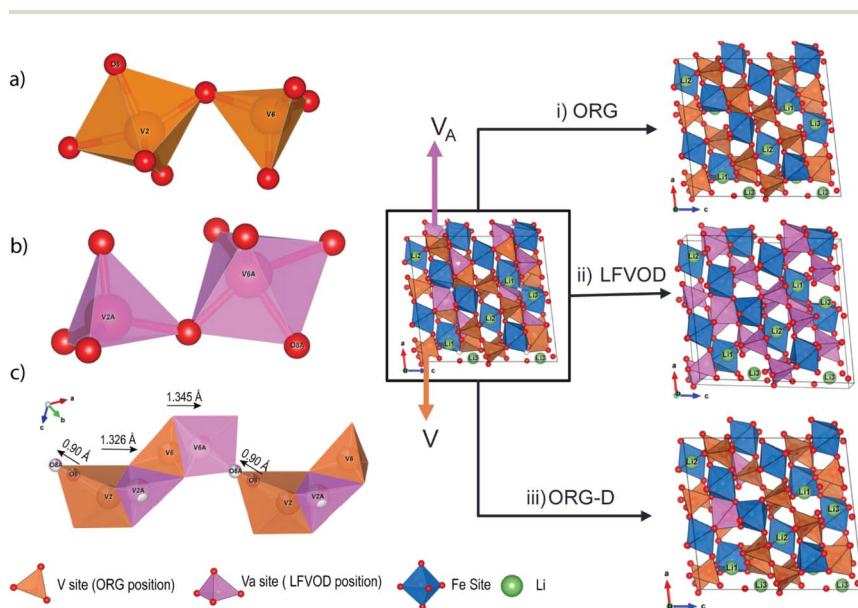
## 3 Results and discussions

Fig. S2† shows an excerpt from our previously reported<sup>17</sup>  $^7\text{Li}$  ssNMR data for  $\text{LiFeV}_2\text{O}_7$  which revealed a complex  $^7\text{Li}$  spectrum for the pristine phase as well as significant changes in the spectra as a function of lithiation.<sup>17</sup> When synthesized using a bulk powder synthesis at  $580^\circ\text{C}$ ,  $\text{LiFeV}_2\text{O}_7$  was found to crystallize in the monoclinic *Cc* space group and consists of extended V–O chains that create layers between which Li and Fe–O units alternate. The lattice parameters are  $a = 13.469(6) \text{ \AA}$ ,  $b = 8.192(4) \text{ \AA}$ ,  $c = 14.390(7) \text{ \AA}$ , and  $\beta = 96.600(9)^\circ$ .<sup>17</sup> It exhibits the presence of two possible local environments for a fraction of 85 and 15% of the vanadium centers. This realization was determined to be the reason for set of signals in the  $^7\text{Li}$  NMR spectrum of the pristine phase. However, more information was needed to give an assignment of the distinct chemical shifts observed in the experimental data, and how they correspond to the local lithium environments. DFT calculations are shown here to be a good approach to providing  $^7\text{Li}$  NMR chemical shift assignments.

### 3.1 Structure optimization

The first step of the calculations, in order to obtain the value of the hyperfine coupling constant, is to optimize the structure of interest. The initial atomic positions were imported from experimental single-crystal diffraction data, then

the structure was optimized using VASP code to yield the most stable atomic arrangement. There are 33 independent atom positions, including three Li sites, three Fe sites, six V sites, and 21 O atomic sites. Fe is displayed as an octahedral  $\text{FeO}_6$  surrounded by five  $\text{VO}_4$  tetrahedra. Fe2 shares the last corner with a  $\text{VO}_5$  trigonal bipyramid while corner-sharing Fe1 and Fe3 share two adjacent edges with the  $\text{VO}_5$  trigonal bipyramid. In the material studied here, two structural models result from the split of V2, V6, and O8 sites into two positions with occupancy of around 85% (named the ORG position<sup>18</sup>) and 15% (named LFVOD position, V2A, V6A, and O8A).<sup>17</sup> The ORG denotes the original position as delineated in the CIF file published by Benabed<sup>18</sup> (Fig. 1a), while LFVOD refers to the vanadium disorder position (Fig. 1b). The difference between the two structures is a small shift of O8A closer toward V6A that changes the coordination environment of V6A into trigonal bipyramidal and V2A into tetrahedra, switching the geometry at both the vanadium sites as shown in Fig. 1c. For this work, we used three different initial positions to create the models: (i) ORG position;<sup>18</sup> (ii) LFVOD position that is related to the disorder position obtained from the new single-crystal analyses reported, and (iii) ORG-D position that combines both positions. For the last one, the position of one asymmetric unit in the ORG structure was changed to a disordered position (LFVOD). This means that the positions of V2, V6, and O8 were changed to V2A, V6A, and O8A, respectively. The structural models consist of supercells comprising four asymmetric unit cells and a total of 132 atoms each. In the ORG-D structure, only three among the 132 atoms were modified to the disorder position, representing localized disordering.



**Fig. 1** (a) Vanadium polyhedral original, (b) disordered position, and (c) the vanadium polyhedral disordered model. Representation of the unit cell for the single-crystal refinement from the [010] direction: (i) ORG position, (ii) LFVOD position, and (iii) ORG-D position, one asymmetric unit in the ORG structure is changed to a disordered position (LFVOD).

Atomic coordinates and cell parameters were fully relaxed, followed by a calculation of the final energy of the optimized geometry. It is well known that there is a self-interaction error associated with GGA strategy, which is related to insufficient localization of electrons on the d-orbital of the transition metal compound. To solve this problem, the generalized gradient approximation with the Hubbard parameter correction (GGA+U) of Dudarev *et al.*<sup>23</sup> was employed. The method applied a unique parameter  $U_{\text{eff}}$  which is the difference between the traditional  $U$  (electron–electron repulsion) and  $J$  (exchange interaction). Some values of  $U_{\text{eff}}$  can be found on the materials project website,<sup>24</sup> where they have calibrated  $U_{\text{eff}}$  values for transition metal oxide systems, for high spin  $\text{Fe}^{3+}$  it is 5.3 eV. However, no  $U_{\text{eff}}$  values have been optimized for  $\text{LiFeV}_2\text{O}_7$ . While a value of 5.3 eV was initially selected as suggested by the materials project,<sup>24</sup> further investigation into the effects of varying  $U$  values on this structure was necessary. Previous studies have shown that  $\text{Li}_3\text{Fe}_2(\text{PO}_4)_3$  (ref. 25) used Hubbard  $U$  values of 3.0 and 4.9 eV for  $\text{Fe}^{3+}$ , while  $\text{Na}_2\text{FePO}_4\text{F}$ <sup>26</sup> used 3.5 and 4.5 eV for  $\text{Fe}^{2+}$ . Motivated by these examples, we decided to test two  $U$  values, 3.5 and 4.3 eV, to see how they affect the electronic structure and the Fermi contact shift. Table 1 shows the results of structural optimization by GGA and GGA+U with  $U_{\text{eff}}$  values of 3.5, 4.3, and 5.3 eV for Fe for all frame models.

All optimized structures showed good agreement with the original reported<sup>18</sup> unit cell. The calculated unit cell parameters exhibited errors of less than 4%. It is worth mentioning that the calculation optimizations were running at 0 K while the experimental results were at room temperature, which can be a source of differences. To a first approximation, the GGA+U approach does not significantly impact the quality of the geometry optimization. However, the difference between the two approaches is evident in the density of states (DOS) plots (Fig. S3†). The plotted total DOS illustrates the orbital occupancies, spin state of the metal and estimates the band gap based on the chosen value of  $U_{\text{eff}}$ . The DOS of Fe 3d orbitals is consistent with the expected high-spin  $\text{Fe}^{3+}$  octahedral configuration, where up spins  $e_g$  and  $t_{2g}$  states are occupied while the down spins are available. As expected, Fig. S3† shows an increase in band gap with addition of  $U_{\text{eff}}$ . As

**Table 1** Relaxed cell parameters for the GGA and GGA+U optimized  $\text{LiFeV}_2\text{O}_7$  from ORG, LFVOD and ORG-D structure unit cell compared to experimental values

Unit cell parameters	$a$ (Å)	$b$ (Å)	$c$ (Å)	Volume (Å <sup>3</sup> )
Exp <sup>18</sup>	13.463	8.1882	14.386	1575.5
LFVOD exp <sup>17</sup>	13.469	8.1924	14.390	1577.2
ORG-GGA	13.654	8.3003	14.148	1631.4
ORG-GGA+U	13.697	8.2647	14.517	1632.4
$U_{\text{eff}} = 5.3$ eV				
ORG-GGA+U	13.675	8.2529	14.497	1625.0
$U_{\text{eff}} = 4.3$ eV				
ORG-GGA+U	13.679	8.2531	14.501	1626.2
$U_{\text{eff}} = 3.5$ eV				
LFVOD-GGA	13.663	8.2393	14.454	1615.8
LFVOD-GGA+U	13.656	8.2261	14.530	1620.8
$U_{\text{eff}} = 5.3$ eV				
ORG-D-GGA+U	13.661	8.2018	14.562	1618.9
$U_{\text{eff}} = 5.3$ eV				

mentioned above, with addition of Hubbard parameter correction ( $U_{\text{eff}}$ ) the electron density is more localized at the TM site, Fe, and the difference between the valence and conduction band is increased. These changes directly affect the Fermi contact shift which is sensitive to how much the unpaired electron spin density is transferred from Fe to Li.<sup>7,9,27</sup>

### 3.2 Fermi contact shift

For paramagnetic samples, the dominant interaction that affects the isotropic shift is the Fermi contact interactions generated by the unpaired electron spin density transferred from the paramagnetic atoms into the observed nucleus. For simple structures, this interaction can be analyzed *via* local geometries and their capability of electron spin transfer based on two mechanisms, spin delocalization and spin polarization.<sup>5,10,11</sup> However, for complicated structures where there are no ideal 90- and 180-degree interactions, the chemical shift assignments cannot be qualitatively assessed. DFT calculations are employed here as a primary method to explain the origin of extra  $^7\text{Li}$  signals in the experimental spectra and assign them for  $\text{LiFeV}_2\text{O}_7$ .

According to the experimental data, we infer that there is a positive electron spin density transferred to the lithium environments due to the large positive chemical shift observed in the  $^7\text{Li}$  NMR spectrum (Fig. 2). The results of calculated  $^7\text{Li}$  Fermi contact shifts for ORG and LFVOD structures are compared to the experimental shift values in Table S1.<sup>†</sup> It is shown that the new position generated by the local disorder generates different values of  $^7\text{Li}$  shifts relative to the original

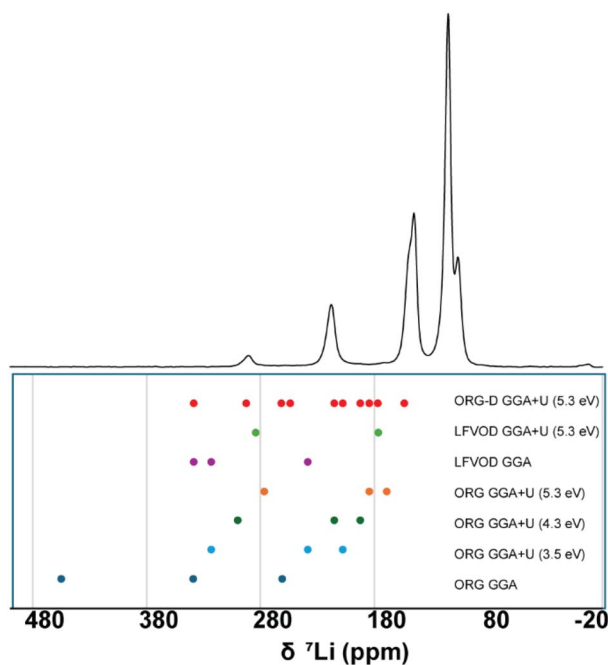


Fig. 2  $^7\text{Li}$  NMR experimental spectrum (top) and DFT calculated  $^7\text{Li}$  Fermi contact NMR shifts (bottom). The data points are color-coded according to the computational method used.



structure. This demonstrates that despite being a small variation at the V2, V6, and O8 positions, the Li environments are affected.

In contrast to our observations during structure optimization, there is a notable difference in the calculated Fermi shift when comparing the results from GGA and GGA+U methods. This variation arises due to the influence of electron localization in the GGA+U method, which significantly impacts the predicted magnitude of electron spin density transfer at the Li sites. For ORG structure, the GGA+U approach provides a more accurate Li shift upon addition and increase of the  $U_{\text{eff}}$  correction term. The increased localization of electron density at Fe minimized the electron spin density transfer to the Li nucleus, which directly affects the Li shift in ssNMR. All values of  $U_{\text{eff}}$  cause a similar effect to the calculated Li shifts (Table S1†). As the value of  $U_{\text{eff}}$  is increased, electrons are more localized in the d orbital which decreases the overlap with the orbital from oxygen. Consequently, the amount of electron spin density transfer from  $\text{Fe}^{3+}$  to Li sites decreases which results in a smaller paramagnetic shift. Based on the calculations results generated for the ORG structure, the most appropriate Hubbard parameter correction value is 5.3 eV for  $\text{Fe}^{3+}$ . This is also applied to the LFVOD structure. Note however, that will still slightly overestimate the shifts and this may be due to either further need of  $U_{\text{eff}}$  optimization or to the fact that we did not consider the magnetic susceptibility of  $\text{LiFeV}_2\text{O}_7$  but approximated it using the value of  $\text{LiFeP}_2\text{O}_7$ .

Comparing the results obtained for the two modeled structures, there are still fewer resonances calculated than observed in the experimental spectra. The lack of structural disorder in the two distinct ORG and LFVOD structures is consistent with the observed result, namely each structure produces a set of three unique lithium sites in the asymmetric unit which are equivalent throughout the whole unit cell, thus only three different lithium shifts were provided for each set of calculations. However, those separate structures do not represent the real material, but rather what we interpret as two possible structures that co-exist in the experimentally synthesized phase. When the disorder is accounted for, as in the case of ORG-D structure, the lithium sites are no longer equivalent resulting in 12

**Table 2** Calculated shifts for Li sites by GGA+U method for the ORG-D structure

ORG-D GGA+U ( $U = 5.3$  eV)

CIF site	Site	Fermi shift $^7\text{Li}$ (ppm)
Li1	Li1 <sub>a</sub>	192.4
Li1	Li1 <sub>b</sub>	153.9
Li1	Li1 <sub>c</sub>	215.5
Li1	Li1 <sub>d</sub>	177.1
Li2	Li2 <sub>a</sub>	338.7
Li2	Li2 <sub>b</sub>	254.0
Li2	Li2 <sub>c</sub>	292.5
Li2	Li2 <sub>d</sub>	261.7
Li3	Li3 <sub>a</sub>	207.8
Li3	Li3 <sub>b</sub>	184.7
Li3	Li3 <sub>c</sub>	177.0
Li3	Li3 <sub>d</sub>	192.4



Li shifts being calculated, shown in Table 2. The reason for this change may be related to bond length, the angles, and the volume of the polyhedron at the lithium site, which can lead to the shortening or stretching of the distance to the transition metal. The best correlation with experimental  $^7\text{Li}$  NMR spectra was thus obtained with the defect structure, ORG-D. Given the DFT calculations results obtained for ORG-D, the most shifted experimental 292 ppm, may be correlated with the calculated shift for  $\text{Li2}_a$  at 338.7 ppm, explaining the presence of a high shift in the experimental  $^7\text{Li}$  NMR. A detailed explanation of the relevant electron spin transfer pathway is described below.

### 3.3 Spin transfer mechanism

In order to assign the Li signals, spin density maps resulting from the difference between up spin and down spin states, were plotted in three dimensions using the VESTA software (Fig. 3). In these maps, only positive spin density is observed as indicated by the presence of yellow surfaces. Based on the electron spin density transfer mechanism, we propose an explanation for shift magnitudes of positive sign of  $^7\text{Li}$  observed for  $\text{LiFeV}_2\text{O}_7$  structures.  $\text{Li2}$  sites are located in a four-coordinated site surrounded by three  $\text{FeO}_6$  octahedra where two are sharing a corner and one sharing an edge with  $\text{LiO}_4$  (Fig. S4†). The unpaired electrons from the three  $\text{Fe}^{3+}$  are the source of electron spin density transfer to Li sites and the cause of high paramagnetic shift. In the case of  $\text{Li1}$  and  $\text{Li3}$ , they are located in a six-coordinated site surrounded by two  $\text{FeO}_6$  octahedra. They are expected to appear at lower paramagnetic shift than  $\text{Li2}$  because they only receive contributions from two  $\text{Fe}^{3+}$ .

Two different spin-transfer mechanisms from Fe to Li are present. (i) For the case that  $\text{FeO}_6$  and  $\text{LiO}_4/\text{LiO}_5$  share a corner, a delocalization mechanism occurs through hybridization between  $\text{Fe } e_g^*$ , O p, and Li s. The electrons in the  $\text{Fe } e_g^*$  orbitals are expected to interact with O p orbitals along the Fe–O–Li pathway through the interaction angle of  $180^\circ$ . In our case, the angles are in the range from  $111.69$  to  $141.72^\circ$  which differs from  $180^\circ$ , but the transfer is still possible. This mechanism can also be observed for  $\text{LiFePO}_4$  and  $\text{LiNi}_2\text{O}_4$ .<sup>9,28</sup> (ii) In the case of  $\text{FeO}_6$  and  $\text{LiO}_4/\text{LiO}_5$  sharing an edge, the delocalization mechanism occurs through hybridization between  $\text{Fe } t_{2g}^*$ , O p, and Li s. The Fe–O–Li angles are in the range from  $93.45$  to  $102.71^\circ$  which only slightly differs from  $90^\circ$ . Based on the

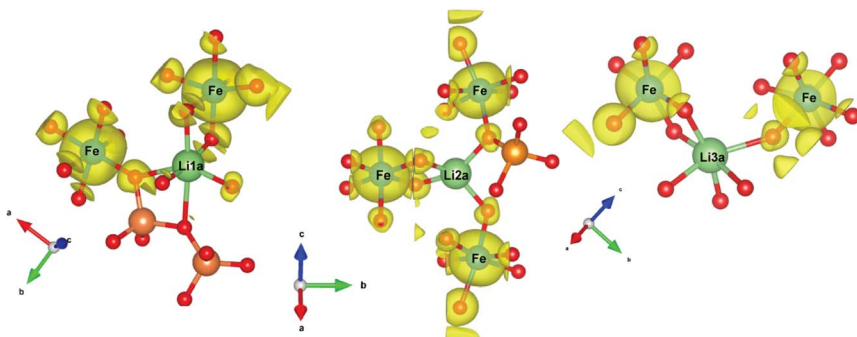


Fig. 3 3D spin density map calculated for ORG-D with GGA+U ( $U_{\text{eff}} = 5.3$  eV) and an isosurface value equal to  $0.005$  spin per  $\text{\AA}^2$ ; yellow surfaces indicate positive spin densities.

results of the ORG-D GGA+U approach, we assigned the experimental  $^7\text{Li}$  NMR spectra as listed in Table 2.

For all modeled structures, Li2 was calculated to be the high chemical shift, due to the three  $\text{Fe}^{3+}$  electron spin density contributions. Conversely, Li1 and Li3, both receive electron spin density transfer from two neighboring  $\text{Fe}^{3+}$ . The distinction in the Fermi contact shifts observed at each lithium site can be attributed to variations in the Fe–Li distance and the Li–O–Fe angle. These geometrical variations directly affect the degree of orbital interaction, consequently adjusting the electron spin transfer magnitude to the lithium sites.

As indicated above, the ORG-D model exhibits the strongest correlation with the experimental  $^7\text{Li}$  NMR spectra. Beyond the number of resonances in the presence of disorder, the experimental shift at 292 ppm closely aligns with the calculated shift for Li2<sub>a</sub> at 338.7 ppm. The introduction of disorder, particularly when V2 occupies a disordered position (V2A), brings it nearer to the lithium site (Li2<sub>a</sub>), and prompts a structural reorganization among surrounding atoms. This adjustment includes a reduction in the Fe2–Li2<sub>a</sub> distance from 3.0421 Å in the ORG model to 3.0020 Å in the ORG-D model. Such a decrease enhances the orbital overlap among the Fe  $t_{2g}^*$ , O p, and Li s orbitals, resulting in a pronounced Fermi contact shift. Tables S2, S3, and S4<sup>†</sup> offer information about calculated Li–Fe distances and Li–O–Fe angles for all modeled structures.

This study elucidates how structural disorders modify lithium environments, leading to significant variations in the electron spin density transfer mechanisms consequently in Fermi contact shifts. The ORG-D model exhibits the closest correlation with experimental NMR spectra, highlighting the relationship between local geometry and electronic interactions.

### 3.4 Structural evolution of $\text{LiFeV}_2\text{O}_7$ during half-cell operation

A comprehensive understanding of structural changes of cathode materials during the process of charge and discharge is crucial for the development of new materials and improving existing ones. For  $\text{LiFeV}_2\text{O}_7$  an increase in local lithium dynamics was observed after 0.5 mol of lithium was inserted into the structure, through the evolution of the  $^7\text{Li}$  NMR spectra *via* both 1D  $^7\text{Li}$  MAS data acquired at 60 kHz MAS and the combination of chemical exchange methods including  $^7\text{Li}$  EXSY and Selective Inversion spectroscopy.<sup>17</sup> Therefore, the chemical composition,  $\text{Li}_{1-x}\text{FeV}_2\text{O}_7$  is an interesting structure that warrants further investigation, to evaluate the unit cell-level changes that facilitate this observed change in lithium dynamics.

**3.4.1 *Operando* SPXRD.** To understand the evolution of the  $\text{Li}_{1-x}\text{FeV}_2\text{O}_7$  structure, *operando* SPXRD is carried out on a half-cell configuration (Fig. S1<sup>†</sup>). Fig. 4 shows a series of SPXRD patterns that were collected during the electrochemical discharge of  $\text{LiFeV}_2\text{O}_7$  vs. Li metal to investigate the structural evolution associated with Li insertion. The cell discharged from 2.75 V to 2.27 V vs.  $\text{Li/Li}^+$ .

The different colored lines in the plot represent diffraction patterns acquired at successive states of discharge. From the bottom to the top of the data series, there is a clear change in the observed reflections coincident with the progression of the discharge process. The series of diffractograms suggests a continuous change in the structure. It is evident that there are shifts in the positions of individual reflections as well as variations in intensity, and the coalescence of

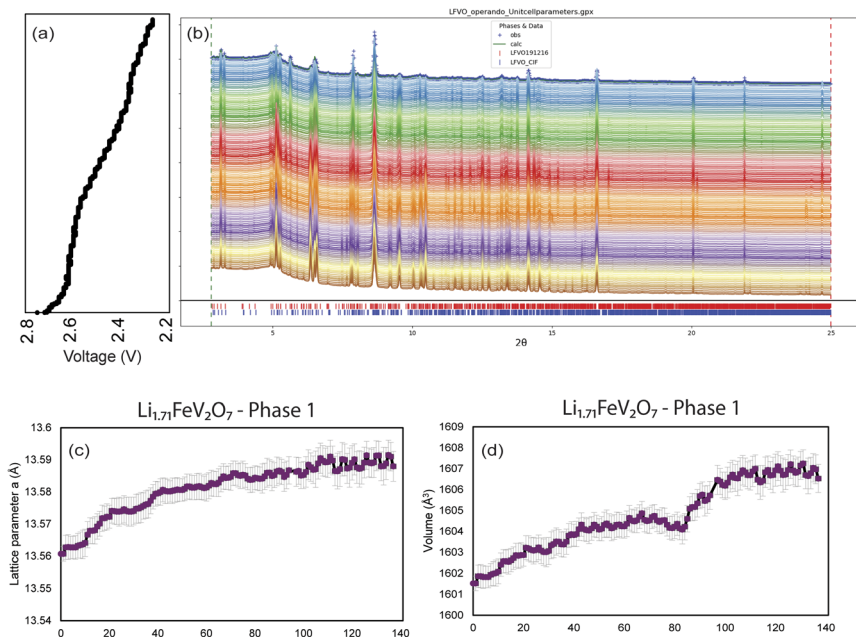


Fig. 4 (a) Voltage profile of first discharge cycle for the *operando* coin cell from 2.75 V to 2.27 V vs. Li/Li<sup>+</sup>; (b) the evolution of the X-ray diffraction patterns of Li<sub>1.71</sub>FeV<sub>2</sub>O<sub>7</sub>; (c) and (d) the plots indicate how the *a* unit cell parameters, and volume, change over time, with error bars indicating the measurement's reliability and precision at each point.

certain peaks as the electrochemical discharge progresses. These changes are indicative of alterations in the crystal structure, suggesting phase transformations or changes in the lattice parameters due to lithium-ion insertion in the material.

The sequential Rietveld refinement of unit cell parameters over the course of the 139 scans for LiFeV<sub>2</sub>O<sub>7</sub> is performed using a two phases model. Even though the second phase is only detected after 0.5 mol of lithium is inserted, we choose to approach the data in this way to monitor the main phase transformation during the lithiated process. Li<sub>*x*</sub>FeV<sub>2</sub>O<sub>7</sub> electrode material undergoes a complex Li<sup>+</sup> insertion mechanism with sequential biphasic and solid-solution reactions during the first discharge process. The complexity of the data, characterized by a large number of peaks and their overlapping plus complex Li<sup>+</sup> insertion mechanism, poses a significant challenge to conducting a detailed analysis. The proximity of many peaks makes it difficult to isolate and analyze individual peak variations with high confidence. Due to these limitations, we focus our analysis on the unit cell parameters evolution during the first discharge cycle for phase 1. This approach provided valuable insights into the structural transformations occurring within the material. Extra information about phase 2 is found in Fig. S5.†

Fig. 4 shows the evolution of the *a*-lattice parameter as well as the unit cell volume for phase 1 during the electrochemical lithiation of Li<sub>1.71</sub>FeV<sub>2</sub>O<sub>7</sub>. Overall, the unit cell volume expands as the experiment progresses, which increases by 0.37% during the lithiation. This phenomenon can be attributed to the increment

in ionic radii of vanadium and iron produced upon Li insertion due to the reduction process and also the amount of lithium inserted. An increase in the unit cell volume often results in larger interstitial spaces within the crystal structure. These spaces can serve as pathways for lithium ions to move more freely through the electrode material resulting in an increase in the lithium dynamics. This result explains why an increase in lithium dynamics was observed in a lithiated sample by  $^7\text{Li}$  NMR.

The *operando* SPXRD data provided a comprehensive overview of the transformations occurring within the unit cell. Nonetheless, the evident modification in the diffraction data exhibited a more gradual progression in comparison to the abrupt change in the  $^7\text{Li}$  NMR spectra. To elucidate the impact of lithium insertion on the local structure with greater clarity, further investigation was conducted through *ex situ* synchrotron X-ray powder diffraction and *ab initio* computational studies.

### 3.5 Structure determination of $\text{Li}_{1.71}\text{FeV}_2\text{O}_7$

**3.5.1 *Ex situ* SPXRD.** In order to obtain a more comprehensive understanding of the phases present during the enhancement of lithium-ion dynamics, the *ex situ* SPXRD pattern of  $\text{Li}_{1.71}\text{FeV}_2\text{O}_7$  was obtained by discharging the half coin cell to 2.39 V vs.  $\text{Li}/\text{Li}^+$ . The Rietveld refinement process involves adjusting the scale, background, and lattice parameters of the reference patterns to align with the experimental peaks, resulting in a low  $R_{\text{wp}}$  value of 4.75%.  $\text{Li}_{1.71}\text{FeV}_2\text{O}_7$  consists of two phases: 65.54% phase 1 and 34.46% phase 2 (Fig. S6†). Although these phases share a similar structural framework, they exhibit slight variations in lattice parameters and are presumed to differ in their lithium content. The coexistence of structurally similar crystal phases with subtle differences in elemental composition can be observed not only in cycled battery materials,<sup>29,30</sup> but also in mineralogical system.<sup>31</sup>

Following lithiation, notable modifications in the lattice dimensions and volume were observed compare to the parent structure, while the crystallographic space group, monoclinic *Cc*, remained unchanged. This indicates that the structural symmetry is preserved even as the framework accommodates extra lithium ions. Table 3 provides the detailed lattice parameters obtained with the Rietveld refinement.

Given the complexity of the material, we narrowed our investigation to the predominant phase, Phase 1, for further investigation. This choice allows for a more in-depth exploration of the phase that plays the most significant role in the interpretation of the  $^7\text{Li}$  NMR spectra. The *ex situ* SPXRD diffractogram pattern

**Table 3** Rietveld refinement unit cell parameters for both phases in the  $\text{Li}_{1.71}\text{FeV}_2\text{O}_7$  compared with the pristine phase

Unit cell parameters	Pristine $\text{LiFeV}_2\text{O}_7$ (ref. 17)	$\text{Li}_{1.71}\text{FeV}_2\text{O}_7$ Phase 1	$\text{Li}_{1.71}\text{FeV}_2\text{O}_7$ Phase 2
$a$ (Å)	13.469(6)	13.594(5)	13.599(9)
$b$ (Å)	8.192(4)	8.250(3)	8.272(6)
$c$ (Å)	14.390(7)	14.216(6)	14.308(6)
$\beta$ (°)	96.600(9)	94.866(5)	95.309(8)
Volume (Å <sup>3</sup> )	1577.2(1)	1588.7(7)	1602.9(2)

does not allow for precise determination of lithium positions. The new lithium sites in  $\text{Li}_{1.71}\text{FeV}_2\text{O}_7$  were deduced from the bond valence energy landscape (BVEL) and then the structures were re-examined by DFT calculations.

**3.5.2 Bond valence energy landscape.** BVEL calculations have been used to predict possible positions for ions and also to prove ion diffusion pathways in diverse materials.<sup>13,32–37</sup> With this approach, BVEL were generated, where valence units are transformed into energy units as implemented in the program BondSTR of the Fullprof Suite.<sup>38</sup> Calculations were made using the soft bond valence parameters developed by S. Adams.<sup>39</sup> This approach considers the polarizability of the mobile species, in this case  $\text{Li}^+$ , and the influence of the counterions of the structure up to a distance of 10 Å. This approach allows for visualizing conduction pathways in the structure while giving hints to possible conduction mechanisms. In our case, these calculations served as a guide for identifying plausible sites for lithium insertion.

Fig. 5 shows the calculated BVEL for  $\text{Li}^+$  conduction pathways in the  $\text{Li}_{1.71}\text{FeV}_2\text{O}_7$  structure phase 1 obtained from the Rietveld refinement with an iso-surfaces value of 0.2 valence units. The yellow iso-surfaces represent the most likely migration route for Li ions. Utilizing VESTA software, we incorporated eight new lithium sites into a structure refined  $\text{Li}_{1.71}\text{FeV}_2\text{O}_7$  guided by the results obtained by BVEL calculations. After inserting the new lithium ions, the modified structure was submitted to geometry optimization by DFT calculation in VASP to get the stable atomic position of the modified structure. The same approach has been used to predict the lithium position in the  $\text{LiH}_2\text{V}_3\text{O}_8$  structure which exhibited agreement with the data obtained with neutron diffraction.<sup>32</sup>

### 3.6 *Ab initio* DFT studies of lithiated sample

Density functional theory (DFT) calculations were conducted in VASP to investigate the stability of the modeled structure and to elucidate the correlation

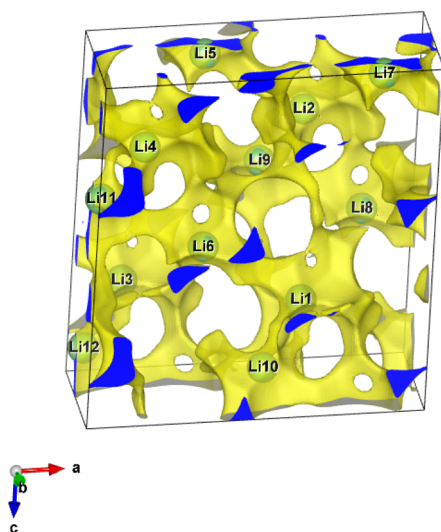


Fig. 5 Bond Valence Energy Landscape (BVEL) calculation for Li-ions in  $\text{Li}_{1.71}\text{FeV}_2\text{O}_7$  phase 1 with the iso-surfaces of 0.2 plotted in VESTA.

between experimental  $^7\text{Li}$  NMR shifts and specific sites within the phases formed during the electrochemical lithiation of  $\text{LiFeV}_2\text{O}_7$ . For the lithiated phase  $\text{Li}_{1.71}\text{FeV}_2\text{O}_7$ , geometry optimization focused on Phase 1, which was identified from the Rietveld refinement of  $\text{Li}_{1.71}\text{FeV}_2\text{O}_7$  and further analyzed for new lithium sites using BVEL calculations. The original structure  $\text{LiFeV}_2\text{O}_7$  contained 12 Li per unit cell, whereas the modeled Phase 1 of  $\text{Li}_{1.71}\text{FeV}_2\text{O}_7$  featured 20 Li. This model served as the basis for structural relaxation, leading to an optimized structure that was subsequently compared with the experimental results in Table S5.† The optimized lattice parameters ( $a$ ,  $b$ , and  $c$ ) obtained *via* the GGA+U method showed a deviation within a 3% error margin when compared with those determined experimentally through the diffraction technique.

As mentioned in the *operando* and *ex situ* SPXRD data, an increase in lattice parameters and unit cell volume suggests more open pathways or larger interstitial sites, providing a reason for increased lithium mobility observed in our previously published NMR data.<sup>17</sup> With the structure optimized, we can have a more detailed understanding of the effects of unit cell changes on lithium dynamics. The Li–Li distances and the size of the channels, or bottlenecks, can significantly affect lithium dynamics in cathode materials for lithium-ion batteries.

Summarized in Table 4, it is possible to compare the lithium dynamics in the pristine and lithiated structure of  $\text{LiFeV}_2\text{O}_7$  using the Li–Li distances and the Li–O bottleneck. Lithium–oxygen (Li–O) bottleneck diffusion area was calculated by the area of the face that the mobile lithium ions share when exchanging with their respective partners. In the pristine structure, the lack of energy barrier data implies that the lithium dynamics were not quantified under the conditions studied. There is a noticeable change in the bottleneck size for the  $\text{Li}_{1\text{B}}\text{--Li}_{2\text{A}}$ , and  $\text{Li}_{1\text{B}}\text{--Li}_{3\text{C}}$  pairs, which increases from 4.32 to 4.48 Å<sup>2</sup> and 3.84 to 4.06 Å<sup>2</sup> respectively. This enlargement of the bottleneck potentially allows for easier lithium-ion movement, contributing to improved lithium dynamics in the lithiated structure.

The Li–Li distances do not change significantly upon lithiation, with only slight variations. This suggests that the average spacing between lithium ions

**Table 4** Summary of activation energy values for the three Li–Li exchange pairs as well as the calculated Li–O bottlenecks of diffusion for pristine and lithiated structures

Pristine	Lithium pair	Energy barrier	Li–Li distance (Å)	Li–O bottleneck (Å <sup>2</sup> )
	$\text{Li}_{1\text{B}}\text{--Li}_{2\text{A}}$	—	4.46	4.32
	$\text{Li}_{1\text{B}}\text{--Li}_{3\text{C}}$	—	3.2	3.84
	$\text{Li}_{2\text{A}}\text{--Li}_{3\text{C}}$	—	4.68	4.86
Lithiated model $\text{Li}_{1.71}\text{FeV}_2\text{O}_7$	Lithium pair	Energy barrier <sup>17</sup>	Li–Li distance (Å)	Li–O bottleneck (Å <sup>2</sup> )
	$\text{Li}_{1\text{B}}\text{--Li}_{2\text{A}}$	$0.59 \pm 0.06$	4.38	4.48
	$\text{Li}_{1\text{B}}\text{--Li}_{3\text{C}}$	$0.48 \pm 0.07$	3.2	4.06
	$\text{Li}_{2\text{A}}\text{--Li}_{3\text{C}}$	$0.4 \pm 0.3$	4.64	4.95

does not drastically impact lithium dynamics after lithiation, at least not to the extent that would be indicated by the Li–Li distances alone. However, it is also notable that a short Li–Li distance facilitates easier lithium hopping between these sites, resulting in a lower energy barrier, as observed for the  $\text{Li}_{1\text{B}}\text{--Li}_{3\text{C}}$  pair. Both interatomic Li distances and bottleneck sizes are important factors to consider for understanding ionic conductivity in cathode material.

All these changes were evidenced by ssNMR spectroscopy, reflecting altered local environments and enhanced dynamics of lithium ions during the discharge process. The NMR data showed these changes through shifts in signal positions, changes in line widths (indicating changes in lithium mobility), and the appearance of a new signal in negative chemical shift, indicating that a new lithium environment was created.

### 3.7 Fermi contact shift and spin transfer mechanism

The calculated spin density of state (DOS) for the optimized phase 1 of  $\text{Li}_{1.71}\text{FeV}_2\text{O}_7$  is given in Fig. 6. Different from what was observed in the pristine material, the plotted DOS for  $\text{Li}_{1.71}\text{FeV}_2\text{O}_7$  shows a change in the relative contributions of the Fe and V in d orbitals suggesting that both are going towards the redox process. The high-spin 3d electron configuration of  $\text{Fe}^{2+}$  ions is confirmed by the appearance of occupied  $e_g$  orbitals and a lift in degeneracy of the  $t_{2g}$  down orbitals, one being occupied. For vanadium ions, which previously did not have any d orbital occupied, now a single unpaired electron is located in the  $t_{2g}$  orbital. In  $\text{LiFeV}_2\text{O}_7$ , there are six vanadium sites situated in two different environments: five of these sites form  $\text{VO}_4$  tetrahedra, while one adopts a [5]-coordinated  $\text{VO}_5$  polyhedral geometry. In the presence of new occupied lithium sites, it is noted that vanadium atoms in 5 coordination are reduced in priority relative to the other vanadium atoms during the lithiation process. This is explained based on the charge compensation and the size of polyhedron to better accommodate the large  $\text{V}^{4+}$  cation. This result confirmed the hypothesis raised by Benabed.<sup>18</sup> Initially, the theoretical capacity of  $\text{LiFeV}_2\text{O}_7$  was calculated assuming one  $\text{Li}^+$  per formula unit,  $97\text{ mA h g}^{-1}$ . However, the measured discharge capacity at the first cycle

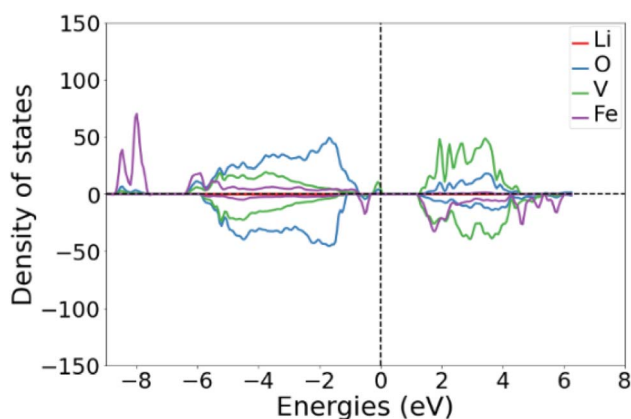


Fig. 6 Calculated total spin DOS for  $\text{Li}_{1.71}\text{FeV}_2\text{O}_7$  with GGAU where the color coding of lines represents elements.



reached 100 mA h g<sup>-1</sup>, which was slightly higher than the theoretical capacity, suggesting that vanadium was also partly reduced.

DFT calculations confirm that the two transition metals are reduced throughout the discharge process. For paramagnetic samples, the dominant interaction that affects the isotropic shift is the Fermi contact interactions and now in addition to the unpaired electrons from Fe<sup>3+</sup>/Fe<sup>2+</sup>, we also have unpaired electrons from V<sup>4+</sup>. The <sup>7</sup>Li ssNMR Fermi contact shift was computed using the GGA+U method and the results can be found in Table S6.† All computed <sup>7</sup>Li Fermi shifts for Li<sub>1.71</sub>FeV<sub>2</sub>O<sub>7</sub> are compared to the experimental spectrum in Fig. 7. The experimental data is characterized by multiple signals, including four intense peaks at 211, 178, 144 and -55 ppm. The signal observed around 0 ppm is attributed to electrolyte. The signals are very broad and thus it is possible for multiple signals to overlap.

In order to understand the electronic spin transfer mechanism from the V<sup>4+</sup> ions to Li<sup>+</sup> in the optimized Li<sub>1.71</sub>FeV<sub>2</sub>O<sub>7</sub> structure, we plotted the calculated 3D spin density map in selected regions of the cell as shown in Fig. 8. The 3D spin density maps of the entire structure can also be found in the ESI (Fig. S7†). The positive and negative electron spins are presented in yellow and blue isosurfaces, respectively. The V<sup>4+</sup> ion exhibits one unpaired electron localized in the d<sub>xy</sub> orbital perpendicular to the V–O–Li axis. The z-direction used to define the orientation of the orbitals was chosen to run along the V2–O10 interatomic axis as shown in Fig. 8. All of them are independent of the *a*, *b*, and *c* crystallographic directions of the unit cell. As seen in Fig. 8, no orbital overlap involves this V<sup>4+</sup> 3d<sub>xy</sub> orbital and the spin density does not point toward Li, the V–O–Li angle is equal to 159.76°. However, as can be seen also in Fig. 8, the O 2p orbital is negatively polarized. This is the case where the electron spin density is transferred to the s orbital *via* a polarization mechanism. The unpaired electron of the partially filled Vt<sub>2g</sub> bands polarizes deeper fully occupied levels resulting from the V<sub>g</sub>–Op–Lis orbitals hybridization leading to a negative electronic spin on Li and consequently to a negative shift for <sup>7</sup>Li NMR.<sup>10,40</sup> This behavior has been seen for V<sup>4+</sup> in other

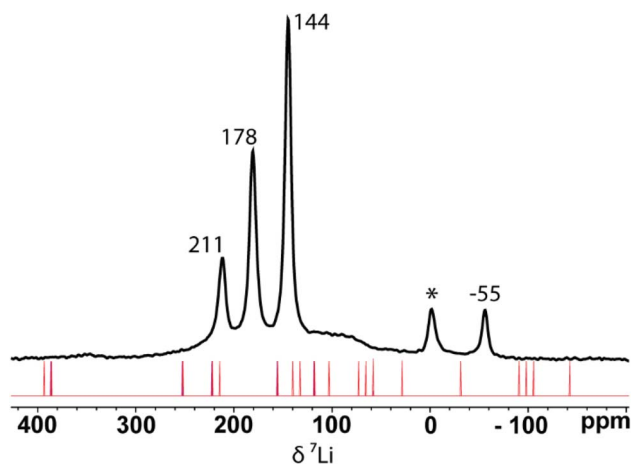


Fig. 7 Comparison between the experimental <sup>7</sup>Li MAS NMR signals of Li<sub>1.71</sub>FeV<sub>2</sub>O<sub>7</sub> and the calculated ones for the modeled supercell. The asterisk indicates the signal from electrolyte residual salt.

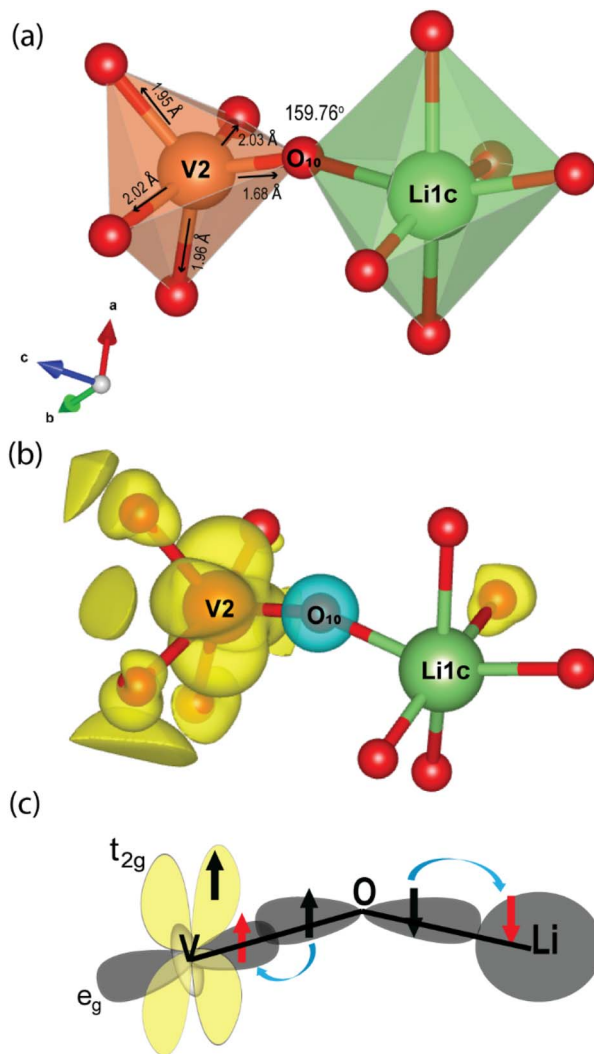


Fig. 8 (a) Local environment of  $V^{4+}$  and  $Li^+$  in  $Li_{1.71}FeV_2O_7$  modeled structure. (b) 3D calculated spin density map showing the electron spin density surrounding a  $V^{4+}$  ion (0.005 spin per  $\text{\AA}^2$  isosurface value). (c) Schematic representation of orbital overlap that results in a negative electronic spin density being transferred to the  $2s$  orbital via a polarization mechanism.

structures, such as  $LiVOPO_4$  (ref. 41) and  $Na_3V_2(PO_4)_2FO_2$ .<sup>6</sup> These results explain the single resonances observed at  $-55$  ppm in the experimental  $^7Li$  NMR spectrum and thus confirm the reduction of  $V^{5+}$  ions upon discharge.

The reduction of vanadium increases the number of paramagnetic species in the structure. The orientation of the vanadium  $d$  orbitals leads to some large shifts compared to the pristine material. However, for the  $Li1_b$  site, the computed Fermi shift is larger than the experimentally observed shifts. With the addition of new lithium sites, the optimized lithiated structure is reorganized decreasing the  $Fe2-V4$  distance from 3.3342 to 2.9906 Å. This structural change alters the

coordination at some vanadium sites from  $\text{VO}_4$  to  $\text{VO}_5$ . Unlike the scenario with  $\text{Li1}_c$ , for this case the orientation of the vanadium d orbital is such that it aligns towards the Li orbital, facilitating a delocalization mechanism that shifts the chemical shift to higher ppm values. Consequently, the lithium site receives electron spin density from both vanadium and iron. This theoretical outcome, however, does not align with experimental observations, suggesting that additional models should be explored for a more accurate representation.

## 4 Conclusion

In conclusion, the research presented provides a comprehensive investigation into the electronic structure and associated  $^7\text{Li}$  NMR chemical shifts of  $\text{LiFeV}_2\text{O}_7$  as a lithium cathode material, utilizing a combination of Density Functional Theory (DFT) calculations and *operando* SPXRD. The study elucidates the influence of defect-associated vanadium atom positioning on the  $^7\text{Li}$  NMR shifts. The computed Fermi shift values for the modeled disordered structure (ORG-D) are in good agreement with the experimental data, showing the sensitivity of NMR spectroscopy to a minimal local alteration. We also examined the structural evolution of  $\text{LiFeV}_2\text{O}_7$  during the lithiation process, correlating it with the dynamics of lithium insertion. The observed volume expansion during the first discharge cycle by *operando* SPXRD contributed to the enhanced lithium dynamics in the bulk material. The lithiated phase  $\text{Li}_{1.71}\text{FeV}_2\text{O}_7$  was analyzed using *ex situ* SPXRD and modeled through BVOL calculations and verified by DFT calculations. Upon comparison between the optimized lithiated structure and its parent framework, an expansion of the bottleneck regions was observed. This structural modification facilitates the movement of lithium ions, significantly enhancing the lithium dynamics within the lithiated structure. Our findings established the involvement of vanadium in the redox processes giving rise to a negative Fermi contact shift through the polarization mechanism. This study shows how ssNMR and DFT calculations are essential tools for gaining detailed insights into the structural intricacies of solid materials. These methodologies are particularly essential for revealing the complexities of local environments and domain structures in oxide materials, such as lithium-ion battery cathodes.

## Conflicts of interest

There are no conflicts to declare.

## Acknowledgements

This research was supported by funding through the NSERC Discovery Grant program, RGPIN-2017-06095, to GRG. Part of the research described in this paper was performed at the Canadian Light Source, a national research facility of the University of Saskatchewan, which is supported by the Canada Foundation for Innovation (CFI), the Natural Sciences and Engineering Research Council (NSERC), the Canadian Institutes of Health Research (CIHR), the Government of Saskatchewan, and the University of Saskatchewan. The Mésocentre de Calcul Intensif Aquitain (MCIA) is acknowledged for computing facilities.

# References

- 1 M. Reynaud, J. Serrano-Sevillano and M. Casas-Cabanas, Imperfect Battery Materials: A Closer Look at the Role of Defects in Electrochemical Performance, *Chem. Mater.*, 2023, **35**(9), 3345–3363, DOI: [10.1021/acs.chemmater.2c03481](#).
- 2 Y. Fan, W. Zhang, Y. Zhao, Z. Guo and Q. Cai, Fundamental Understanding and Practical Challenges of Lithium-Rich Oxide Cathode Materials: Layered and Disordered-Rocksalt Structure, *Energy Storage Mater.*, 2021, **40**, 51–71, DOI: [10.1016/j.ensm.2021.05.005](#).
- 3 S. P. Chen, D. Lv, J. Chen, Y. H. Zhang and F. N. Shi, Review on Defects and Modification Methods of  $\text{LiFePO}_4$  Cathode Material for Lithium-Ion Batteries, *Energy Fuels*, 2022, **36**(3), 1232–1251, DOI: [10.1021/acs.energyfuels.1c03757](#).
- 4 R. Wang, X. Chen, Z. Huang, J. Yang, F. Liu, M. Chu, T. Liu, C. Wang, W. Zhu, S. Li, S. Li, J. Zheng, J. Chen, L. He, L. Jin, F. Pan and Y. Xiao, Twin Boundary Defect Engineering Improves Lithium-Ion Diffusion for Fast-Charging Spinel Cathode Materials, *Nat. Commun.*, 2021, **12**(1), 3085, DOI: [10.1038/s41467-021-23375-7](#).
- 5 D. Carlier, M. Ménétrier, C. Delmas, C. P. Grey and G. Ceder, Understanding the NMR Shifts in Paramagnetic Transition Metal Oxides Using Density Functional Theory Calculations, *Phys. Rev. B: Condens. Matter Mater. Phys.*, 2003, **67**(17), 174103, DOI: [10.1103/PhysRevB.67.174103](#).
- 6 L. H. B. Nguyen, P. S. Camacho, T. Broux, J. Olchowka, C. Masquelier, L. Croguennec and D. Carlier, Density Functional Theory-Assisted  $^{31}\text{P}$  and  $^{23}\text{Na}$  Magic-Angle Spinning Nuclear Magnetic Resonance Study of the  $\text{Na}_3\text{V}_2(\text{PO}_4)_2\text{F}_3\text{--Na}_3\text{V}_2(\text{PO}_4)_2\text{FO}_2$  Solid Solution: Unraveling Its Local and Electronic Structures, *Chem. Mater.*, 2019, **31**(23), 9759–9768, DOI: [10.1021/acs.chemmater.9b03546](#).
- 7 T. Bamine, E. Boivin, F. Boucher, R. J. Messinger, E. Salager, M. Deschamps, C. Masquelier, L. Croguennec, M. Ménétrier and D. Carlier, Understanding Local Defects in Li-Ion Battery Electrodes through Combined DFT/NMR Studies: Application to  $\text{LiVPO}_4\text{F}$ , *J. Phys. Chem. C*, 2017, **121**(6), 3219–3227, DOI: [10.1021/acs.jpcc.6b11747](#).
- 8 J. Serrano-Sevillano, D. Carlier, A. Saracibar, J. M. Lopez Del Amo and M. Casas-Cabanas, DFT-Assisted Solid-State NMR Characterization of Defects in  $\text{Li}_2\text{MnO}_3$ , *Inorg. Chem.*, 2019, **58**(13), 8347–8356, DOI: [10.1021/acs.inorgchem.9b00394](#).
- 9 A. Castets, D. Carlier, Y. Zhang, F. Boucher and M. Ménétrier, A DFT-Based Analysis of the NMR Fermi Contact Shifts in Tavorite-like  $\text{LiMPO}_4\cdot\text{OH}$  and  $\text{MPO}_4\cdot\text{H}_2\text{O}$  ( $\text{M} = \text{Fe}, \text{Mn}, \text{V}$ ), *J. Phys. Chem. C*, 2012, **116**(34), 18002–18014, DOI: [10.1021/jp302549s](#).
- 10 A. J. Pell, G. Pintacuda and C. P. Grey, Paramagnetic NMR in Solution and the Solid State, *Prog. Nucl. Magn. Reson. Spectrosc.*, 2019, **111**, 1–271, DOI: [10.1016/j.pnmrs.2018.05.001](#).
- 11 J. Kim, D. S. Middlemiss, N. A. Chernova, B. Y. X. Zhu, C. Masquelier and C. P. Grey, Linking Local Environments and Hyperfine Shifts: A Combined Experimental and Theoretical  $^{31}\text{P}$  and  $^7\text{Li}$  Solid-State NMR Study of

- Paramagnetic Fe(III) Phosphates, *J. Am. Chem. Soc.*, 2010, **132**(47), 16825–16840, DOI: [10.1021/ja102678r](https://doi.org/10.1021/ja102678r).
- 12 I. D. Brown, Recent Developments in the Methods and Applications of the Bond Valence Model, *Chem. Rev.*, 2009, **109**(12), 6858–6919, DOI: [10.1021/cr900053k](https://doi.org/10.1021/cr900053k).
  - 13 Z. Zhang, M. Avdeev, H. Chen, W. Yin, W. H. Kan and G. He, Lithiated Prussian Blue Analogues as Positive Electrode Active Materials for Stable Non-Aqueous Lithium-Ion Batteries, *Nat. Commun.*, 2022, **13**(1), 7790, DOI: [10.1038/s41467-022-35376-1](https://doi.org/10.1038/s41467-022-35376-1).
  - 14 M. Manawan, E. Kartini and M. Avdeev, Visualizing Lithium Ions in the Crystal Structure of  $\text{Li}_3\text{PO}_4$  by *in Situ* Neutron Diffraction, *J. Appl. Crystallogr.*, 2021, **54**(5), 1409–1415, DOI: [10.1107/s1600576721008700](https://doi.org/10.1107/s1600576721008700).
  - 15 J. Hafner, Materials Simulations Using VASP—a Quantum Perspective to Materials Science, *Comput. Phys. Commun.*, 2007, **177**, 6–13, DOI: [10.1016/j.cpc.2007.02.045](https://doi.org/10.1016/j.cpc.2007.02.045).
  - 16 R. Hafner, *Ab-Initio* Simulations of Materials Using VASP: Density-Functional Theory and Beyond, *J. Comput. Chem.*, 2008, **29**(13), 2044–2078, DOI: [10.1002/jcc.21057](https://doi.org/10.1002/jcc.21057).
  - 17 T. L. E. Pereira, K. J. Sanders, D. L. Smiley, J. F. Britten and G. R. Goward, Structural Complexity and Evolving Lithium-Ion Dynamics within the Cathode Material  $\text{LiFeV}_2\text{O}_7$  Revealed by Diffraction and Solid-State NMR, *Chem. Mater.*, 2022, **34**(19), 8551–8560, DOI: [10.1021/acs.chemmater.2c01357](https://doi.org/10.1021/acs.chemmater.2c01357).
  - 18 Y. Benabed, L. Castro, N. Penin, J. Darriet and M. Dollé, Synthesis, Structure, and Electrochemical Properties of  $\text{LiFeV}_2\text{O}_7$ , *Chem. Mater.*, 2017, **29**(21), 9292–9299, DOI: [10.1021/acs.chemmater.7b03271](https://doi.org/10.1021/acs.chemmater.7b03271).
  - 19 D. Riou, N. Nguyen, R. Benloucif and B. Raveau,  $\text{LiFeP}_2\text{O}_7$ : Structure and Magnetic Properties, *Mater. Res. Bull.*, 1990, **25**(11), 1363–1369, DOI: [10.1016/0025-5408\(90\)90218-Q](https://doi.org/10.1016/0025-5408(90)90218-Q).
  - 20 K. Momma and F. Izumi, VESTA: A Three-Dimensional Visualization System for Electronic and Structural Analysis, *J. Appl. Crystallogr.*, 2008, **41**(3), 653–658, DOI: [10.1107/S0021889808012016](https://doi.org/10.1107/S0021889808012016).
  - 21 B. H. Toby and R. B. Von Dreele, GSAS-II: The Genesis of a Modern Open-Source All Purpose Crystallography Software Package, *J. Appl. Crystallogr.*, 2013, **46**(2), 544–549, DOI: [10.1107/S0021889813003531](https://doi.org/10.1107/S0021889813003531).
  - 22 A. F. G. Leontowich, A. Gomez, B. D. Moreno, D. Muir, D. Spasyuk, G. King, J. W. Reid, C. Y. Kim and S. Kycia, The Lower Energy Diffraction and Scattering Side-Bounce Beamline for Materials Science at the Canadian Light Source, *J. Synchrotron Radiat.*, 2021, **28**, 961–969, DOI: [10.1107/S1600577521002496](https://doi.org/10.1107/S1600577521002496).
  - 23 S. Dudarev, G. Botton, S. Savrasov, C. Humphreys and A. Sutton, Electron-energy-loss spectra and the structural stability of nickel oxide: An LSDA+U study, *Phys. Rev. B: Condens. Matter Mater. Phys.*, 1998, **57**, 1505.
  - 24 *The Materials Project*, <https://next-gen.materialsproject.org/>.
  - 25 A. Castets, D. Carlier, K. Trad, C. Delmas and M. Ménétrier, Analysis of the  $^7\text{Li}$  NMR Signals in the Monoclinic  $\text{Li}_3\text{Fe}_2(\text{PO}_4)_3$  and  $\text{Li}_3\text{V}_2(\text{PO}_4)_3$  Phases, *J. Phys. Chem. C*, 2010, **114**(44), 19141–19150, DOI: [10.1021/jp106871z](https://doi.org/10.1021/jp106871z).
  - 26 D. L. Smiley, D. Carlier and G. R. Goward, Combining Density Functional Theory and  $^{23}\text{Na}$  NMR to Characterize  $\text{Na}_2\text{FePO}_4\text{F}$  as a Potential Sodium Ion

- Battery Cathode, *Solid State Nucl. Magn. Reson.*, 2019, **103**, 1–8, DOI: [10.1016/j.ssnmr.2019.07.001](https://doi.org/10.1016/j.ssnmr.2019.07.001).
- 27 D. Carlier, M. Ménétrier and C. Delmas, Transferred Hyperfine Interaction between a Tetrahedral Transition Metal and Tetrahedral Lithium:  $\text{Li}_6\text{CoO}_4$ , *J. Phys. Chem. C*, 2010, **114**(10), 4749–4755, DOI: [10.1021/jp911364w](https://doi.org/10.1021/jp911364w).
  - 28 C. Chazel, M. Ménétrier, D. Carlier, L. Croguennec and C. Delmas, DFT Modeling of NMR Contact Shift Mechanism in the Ideal  $\text{LiNi}_2\text{O}_4$  Spinel and Application to Thermally Treated Layered  $\text{Li}_{0.5}\text{NiO}_2$ , *Chem. Mater.*, 2007, **19**(17), 4166–4173, DOI: [10.1021/cm070324n](https://doi.org/10.1021/cm070324n).
  - 29 S. M. Bak, Z. Shadike, R. Lin, X. Yu and X. Q. Yang, In Situ/Operando Synchrotron-Based X-Ray Techniques for Lithium-Ion Battery Research, *NPG Asia Mater.*, 2018, **10**(7), 563–580, DOI: [10.1038/s41427-018-0056-z](https://doi.org/10.1038/s41427-018-0056-z).
  - 30 M. H. Tahmasebi and M. N. Obrovac, Quantitative Measurement of Compositional Inhomogeneity in NMC Cathodes by X-Ray Diffraction, *J. Electrochem. Soc.*, 2023, **170**(8), 080519, DOI: [10.1149/1945-7111/acefff](https://doi.org/10.1149/1945-7111/acefff).
  - 31 S. M. Antao, The Mystery of Birefringent Garnet: Is the Symmetry Lower than Cubic?, *Powder Diffr.*, 2013, **28**(4), 281–288, DOI: [10.1017/S0885715613000523](https://doi.org/10.1017/S0885715613000523).
  - 32 A. Kuhn, J. C. Pérez-Flores, J. Prado-Gonjal, E. Morán, M. Hoelzel, V. Díez-Gómez, I. Sobrados, J. Sanz and F. García-Alvarado, Lithium Intercalation Mechanism and Critical Role of Structural Water in Layered  $\text{H}_2\text{V}_3\text{O}_8$  High-Capacity Cathode Material for Lithium-Ion Batteries, *Chem. Mater.*, 2022, **34**(2), 694–705, DOI: [10.1021/acs.chemmater.1c03283](https://doi.org/10.1021/acs.chemmater.1c03283).
  - 33 L. Lander, G. Rousse, A. M. Abakumov, M. Sougrati, G. Van Tendeloo and J. M. Tarascon, Structural, Electrochemical and Magnetic Properties of a Novel  $\text{KFeSO}_4\text{F}$  Polymorph, *J. Mater. Chem. A*, 2015, **3**(39), 19754–19764, DOI: [10.1039/c5ta05548b](https://doi.org/10.1039/c5ta05548b).
  - 34 L. Lander, M. Reynaud, J. Carrasco, N. A. Katcho, C. Bellin, A. Polian, B. Baptiste, G. Rousse and J. M. Tarascon, Unveiling the Electrochemical Mechanisms of  $\text{Li}_2\text{Fe}(\text{SO}_4)_2$  Polymorphs by Neutron Diffraction and Density Functional Theory Calculations, *Phys. Chem. Chem. Phys.*, 2016, **18**(21), 14509–14519, DOI: [10.1039/c6cp02175a](https://doi.org/10.1039/c6cp02175a).
  - 35 Z. Zou, N. Ma, A. Wang, Y. Ran, T. Song, B. He, A. Ye, P. Mi, L. Zhang, H. Zhou, Y. Jiao, J. Liu, D. Wang, Y. Li, M. Avdeev and S. Shi, Identifying Migration Channels and Bottlenecks in Monoclinic NASICON-Type Solid Electrolytes with Hierarchical Ion-Transport Algorithms, *Adv. Funct. Mater.*, 2021, **31**(49), 2107747, DOI: [10.1002/adfm.202107747](https://doi.org/10.1002/adfm.202107747).
  - 36 J. E. Auckett, L. Lopez-Odrizola, S. J. Clark and I. R. Evans, Exploring the Nature of the Fergusonite-Scheelite Phase Transition and Ionic Conductivity Enhancement by  $\text{Mo}^{6+}$  doping in  $\text{LaNbO}_4$ , *J. Mater. Chem. A*, 2021, **9**(7), 4091–4102, DOI: [10.1039/d0ta07453e](https://doi.org/10.1039/d0ta07453e).
  - 37 R. Xiao, H. Li and L. Chen, High-Throughput Design and Optimization of Fast Lithium Ion Conductors by the Combination of Bond-Valence Method and Density Functional Theory, *Sci. Rep.*, 2015, **5**, 14227, DOI: [10.1038/srep14227](https://doi.org/10.1038/srep14227).
  - 38 J. Rodríguez-Carvajal, *FullProfSuite*.
  - 39 S. Adams, From Bond Valence Maps to Energy Landscapes for Mobile Ions in Ion-Conducting Solids, *Solid State Ionics*, 2006, **177**(19–25), 1625–1630, DOI: [10.1016/j.ssi.2006.03.054](https://doi.org/10.1016/j.ssi.2006.03.054).

- 40 C. P. Grey and N. Dupré, NMR Studies of Cathode Materials for Lithium-Ion Rechargeable Batteries, *Chem. Rev.*, 2004, **104**(10), 4493–4512, DOI: [10.1021/cr020734p](#).
- 41 S. Britto, I. D. Seymour, D. M. Halat, M. F. V. Hidalgo, C. Siu, P. J. Reeves, H. Zhou, N. A. Chernova, M. S. Whittingham and C. P. Grey, Evolution of Lithium Ordering with (de)-Lithiation in  $\beta$ -LiVOPO<sub>4</sub>: Insights through Solid-State NMR and First Principles DFT Calculations, *J. Mater. Chem. A*, 2020, **8**(11), 5546–5557, DOI: [10.1039/d0ta00121j](#).